ELSEVIER

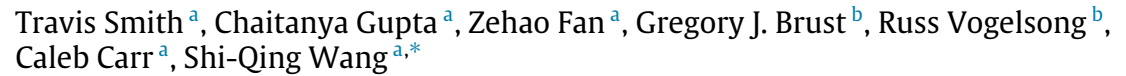
Contents lists available at ScienceDirect

Extreme Mechanics Letters

journal homepage: www.elsevier.com/locate/eml



Toughness arising from inherent strength of polymers





b Wire & Cable USMCA, Lion Elastomers, Baton Rouge, LA 708805, United States of America



ARTICLE INFO

Article history: Received 22 February 2022 Received in revised form 17 April 2022 Accepted 7 June 2022 Available online 16 June 2022

Keywords: Fracture mechanics Inherent strength Plastics Elastomers Birefringence Intrinsic flaws

ABSTRACT

This study carries out spatial-resolved optical birefringence observations to quantify, for mode I (tensile opening) loading, the stress intensification at crack tip of brittle and ductile glassy polymers (polymethyl methacrylate–PMMA, polyethylene terephthalate–PET) as well as one type of elastomer: (ethylene propylene diene monomer–EPDM). We measure the stress buildup in a precut specimen by correlating retardation with the corresponding tensile stress. Given the adequate spatial resolution under 10 μ m and natural bluntness of intentional through-cuts, we are able to show that (a) during drawing at different stages up to the onset of fracture in precut PMMA and EPDM, the local stress saturates, namely, ceases to increase as $r^{-1/2}$ upon approaching the cut tip (with r reaching r_{ss} in a range of 0.05–0.15 mm), (b) tip stress σ_{tip} , i.e., the tensile stress in the stress saturation zone ($r \leq r_{ss}$), linearly grows with (operationally defined) stress intensity factor K_1 until fracture, reaching a level below the breaking stress σ_b observed of uncut specimen. Thus, the inherent strength $\sigma_{F(inh)}$ under plane strain, taken to be the tip stress at fracture is only comparable to σ_b . Moreover, a characteristic length P, involved in the observed linearity between K_1 and σ_{tip} , i.e., in $K_1 = \sigma_{tip} P^{1/2}$, is found to be comparable to $2\pi r_{ss}$. Here r_{ss} appears to depend on the tip sharpness, which may be characterized by a radius of curvature ρ_{tip} . Thus, toughness given by the critical stress intensity factor K_1c is determined by the product of $\sigma_{F(inh)}$ and $\rho_{tip}^{1/2}$, and the critical energy release rate G_{lc} is given by the product of specific work of fracture $w_F = [\sigma_{F(inh)}]^2/2E$ and ρ_{tip} .

© 2022 Elsevier Ltd. All rights reserved.

1. Introduction

Mechanical characteristics of polymeric materials are unique relative to other materials in several ways. Polymers, in either plastic or elastomeric form, can tolerate high strain without fracture because of the global structural connectivity through chain network. For polymers to find more applications and for new, more sustainable polymers to replace conventional polymers, a detailed relationship between polymer structure and mechanical behavior needs to be worked out. However, despite decades of extensive research, a quantitative and predictive chain-level description of key mechanical features of polymers such as ductility, brittle-ductile transition, and toughness against fracture remains intractable to derive from first principles. Specifically, it is still formidable to theoretically estimate the inherent fracture strength $\sigma_{F(inh)}$ of a glassy polymer or an elastomer (made of a crosslinked melt). The upper theoretical bound of inherent strength in excess of 10 GPa for glassy polymers (achievable in polymer fibers) has led researchers to speculate that the observed

E-mail address: swang@uakron.edu (S.-Q. Wang).

brittle stress σ_b may not reflect the inherent strength. Similarly, it is elusive that elastomers typically only show tensile strength on the order of 10 MPa, far lower than a theoretical estimate of several GPa that assumes all load-bearing strands to undergo scission at the same time.

Like the case of silica glasses treated by Griffith [1], for brittle polymers presence of crack of length a lowers the critical far-field stress $\sigma_{\rm c}$ for fracture according to $\sigma_{\rm c} \sim a^{-1/2}$. As a decreases, $\sigma_{\rm c}$ increases until $\sigma_{\rm b}$, which is the fracture strength (breaking stress) of cut-free samples. In the polymer literature, summarized in several monographs, [2–4] brittle fracture of cut-free specimen is usually explained by assuming existence of intrinsic flaws of size a^* so that the Griffith style energy balance argument can be applied to relate the critical energy release rate $G_{\rm lc}$ (i.e., loss of stored energy per unit area upon fracture) to $\sigma_{\rm b}$ as

$$\sigma_{\rm b} = (EG_{\rm lc}/\pi \, a^*)^{1/2}.\tag{1}$$

While σ_b can be directly measured in a tensile test, neither G_{lc} nor a^* is known *a priori*. In practice, a large through-cut of length a is intentionally introduced for the same material so that its toughness G_{lc} can be determined from its operational

^{*} Corresponding author.

definition:

$$G_{\rm Ic} = \pi \sigma_c^2 a / E, \tag{2}$$

where *E* is the Young's modulus.

For brittle PMMA [5] and PS [6], precut specimens were drawn by Berry to fracture and shown to have $G_{Ic} = 0.6 \text{ kJ/m}^2$ and 3.4 kJ/m² respectively. Given $\sigma_b = \text{ca. } 60 \text{ and } 45 \text{ MPa}$, and E = 1.7 GPa and 2 GPa for PMMA and PS respectively, the unknown length scale a^* becomes known from Eq. (1): $a^* =$ $EG_{lc}/\pi\sigma_{b}^{2} = 0.09$ mm for PMMA and 1.0 mm for PS. When intentional through-cut decreases in size to a^* , fracture has been observed [4–6] to take place at σ_c that is comparable to σ_b . Such evidence has allowed the textbook [4] to conclude that there are intrinsic flaws of size a^* . Although a^* in the range of 0.1 to 1 mm is sufficiently large for optical inspection to detect, flaws on such a length scale are usually not observed, thus casting doubt on whether fracture behavior of PMMA and PS should be described in terms of Eq. (1) and questioning the concept of a^* for these polymers. Moreover, because $G_{\rm lc}$ is a thousand times higher than the surface fracture energy Γ , fracture criterion can no longer be formulated as $G_{\rm lc} = \Gamma$. Thus, the Griffith-Irwin style energy balance argument seems to face a major dilemma for polymers, causing one to question whether Eq. (2) is a useful fracture criterion for such polymers.

On the other hand, there is no difficulty to perceive brittle fracture in a uniform defect/flaw-free or flaw-tolerant solid. For example, it is a well-defined theoretical problem to estimate inherent fracture strength σ^* under plane stress or σ^\dagger under plane strain of brittle glassy polymers in absence of any foreign inclusions or cracks—we will subsequently label the inherent strength as $\sigma_{F(inh)}$ when the type of deformation is unspecified. Specifically, according to a recent chain-level phenomenological model [7], $\sigma_{F(inh)}$ at brittle-ductile transition (BDT) scales linearly with the areal density ψ_{LBS} of load-bearing strands (LBS) that characterizes the structure of chain networking: $\sigma_{\text{F(inh)}} = \psi_{\text{LBS}} f_{\text{cp}}$, where f_{cp} represents the critical force for chain pullout by which (rather than chain scission [8]) the chain network undergoes structural breakdown. Thus, the classic Vincent plot [9] acquired a new interpretation: the breaking stress σ_b at BDT is proportional to the bond areal density ϕ because ψ_{LBS} has the same scaling as $\phi = 1/pl_K$ [10], where p and l_K are the packing and Kuhn lengths respectively. Flaw-free uncut specimens show brittle fracture when the chain network is unable to retain its structural integrity during its attempt to bring about activation below BDT. Here f_{cp} is plausibly only a small fraction of the bond breaking strength, which is on the order of several nano-Newtons, and ψ_{LBS} is plausibly only a small fraction of ϕ . Therefore σ^* could only reach a level of 100 MPa, comparable to the experimental measurement of σ_b . If this is the case, it would not require the machinery of fracture mechanics to understand brittle fracture of cut-free polymers.

The preceding discussion pertains to fracture of elastomers as well. Is the observed tensile strength an actual manifestation of their inherent strength? Why is their strength so low or what determines the strength? Has Lake-Thomas model [11] for $G_{\rm Ic}$ captured characteristics of elastomer fracture? Do all elastomeric materials also require us to apply fracture mechanics to describe fracture behavior by postulating existence of intrinsic flaws?

The present study applies birefringence measurements to probe the local stress field in front of a precut during tensile drawing of two glassy polymers and one elastomer, aiming to find out whether, how and why there is an alternative fracture criterion given in terms of explicit stress state at crack tip. Our birefringence observations of precut specimens indicate that (a) intentional through-cut causes stress buildup in linear proportion to the far-field stress σ_0 , e.g., the tip stress increasing linearly

with σ_0 , (b) the tip stress at fracture is below the breaking stress σ_b observed from cut-free specimens, (c) during drawing, i.e., at each value of σ_0 , the local stress tends to saturate upon approaching the tip, revealing a stress saturation zone of size $r_{\rm ss}$, which appears to be related to the cut sharpness characterized by the radius of curvature $\rho_{\rm tip}$ at the cut tip.

2. Experimental and technical backgrounds

2.1. Sample preparation

Three polymer films were studied in this work: PET from Auriga Polymers Inc., PMMA from Professional Plastics. The ethylene propylene diene monomer (EPDM) sheets with thickness 2–2.5 mm were crosslinked at Lion Elastomers with Royalene 511 EPDM, tri-functional crosslinker SR-350 (1 \sim 3 phr), and peroxide DiCup R (3 \sim 4 phr), cured at 170 °C for 20 min.

Dogbone- and stripe-shaped specimens were prepared by first tracing a design onto the sheets and then, for PET, cutting with scissors and paper trimmer to carefully avoid introducing substantial edge defects; for PMMA, removing excess material with a coarse sanding belt and then smoothing the edges with a flat file; for EPDM, simply cutting with paper trimmer along the tracing marker. Dogbone-shaped specimens were employed to obtain the stress-optical relationship and stripe-shaped specimens to study the effect of single-edge notch (SEN).

SEN was introduced to specimens by several means. PET specimens were chilled in a freezer ($-20\,^{\circ}$ C) for 15–30 min, then cut with a similarly chilled nail clipper while still in the freezer. Rapid application of force with the nail clipper generated a thin crack that spontaneously propagated further across the sheet. Crack was introduced in PMMA specimens at room temperature by hammering a glass-scrapper against the side of the sheet. Cut was made in EPDM stripes by pushing the edge of a thin razor blade into the specimens. Tensile extension of uncut and cut specimens was carried out at room temperature on an Instron 5969 tensile tester between crossed polarizer films from Polarization.com. The setup is illustrated in Fig. 1. The reported draw ratio L/L_0 is based on the initial length L_0 of the narrow section of the dogbone specimens and the inter-clamp distance for the stripe specimens respectively.

2.2. Birefringence methods

2.2.1. Setups

The birefringence setup in Fig. 1 allows us to observe the evolution of colors or fringe orders due to increasing birefringence at various corresponding stresses. Given the weak strain-induced birefringence in PMMA a negative retardation plate of 600 nm places the PMMA at retardance of 600 nm at $L/L_0=1$ so that the retardance travels to higher order in the Michel-Levy chart—PMMA shows negative birefringence at room temperature [12, 13]. Because PET is highly birefringent, a negative retardation plate is similarly placed between the polarizer and the sample to avoid color saturation. EPDM shows more than ten orders of retardance. Thus, it is more effective and accurate to use a monochromatic light source (low pressure sodium lamp) and count the order of fringes.

During drawing, the development of birefringence is captured by video recording, involving a variety of cameras and lenses: for PMMA, in order to capture videos at high resolution, a 4K video camera (Mokose C100) was used with a zoom lens (Edmund Industrial Optics) that was employed at $2.5\times$ magnification; for PET, a generic CCD camera was outfitted with the same variable magnification lens at $2.5\times$ magnification; for EPDM, the same 4K video camera was used along with a C-mount zoom-lens (Hayear

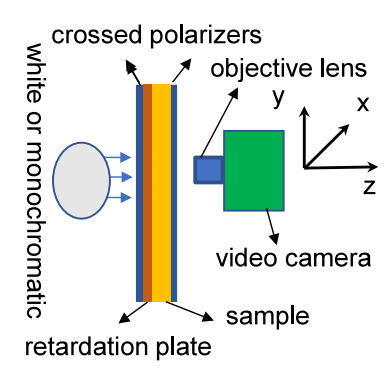


Fig. 1. Sketch of a birefringence setup based on white light for measurement of spatial retardance field, involving two crossed polarizers and a retardation plate that is either arranged to cancel or add to the emergent retardance due to drawing along *y* axis. (For interpretation of the references to color in this figure legend, the reader is referred to the web version of this article.)

model HY-180XA) set at $4.5 \times$. Color information in such videos is digitally stored in an 8-bit Red–Green–Blue (RGB) color space, where every color can be described as a unique combination of R, G and B values, each bearing a value between 0–255.

2.2.2. Stress-optical relation

In glassy polymers and elastomers, there generally exists an explicit (linear) relationship between stress and birefringence arising from the molecular orientation that has a one-to-one correspondence with the stress. Consequently, we can quantify the stress through quantitative measurement of birefringence to obtain tensile stress $\Delta\sigma = \Delta n/C$, where C is stress-optical coefficient. For example, Fig. 2a and Fig. 2b show such a correlation between the retardation (RGB) and corresponding stress during drawing of uncut PMMA and PET respectively. Similarly, the order of fringes N represents the birefringence Δn through

$$\Delta \mathbf{n} = N(\lambda/t) \tag{3}$$

that is directly related to the principal stress difference $\Delta\sigma$. In Eq. (3), t is the specimen thickness and λ is the wavelength of the monochromatic light. By subjecting an uncut EPDM specimen to uniaxial drawing and counting N at the corresponding Cauchy stress we can use Eq. (3) to establish a relationship between Δ n and $\Delta\sigma$ as shown in Fig. 2c. Fig. 2c confirms a linear stress-optical relation (SOR)

$$\Delta \mathbf{n} = \mathbf{C} \Delta \sigma, \tag{4}$$

with $C = 2.2 \times 10^{-9} \, (Pa^{-1})$ for EPDM. Fracture in this specimen occurs when N reaches 14, corresponding to the last data point in Fig. 2c and in its inset. Video-uncut EPDM in the Supporting Information recorded the birefringence as a function of time and revealed that the birefringence actually turned somewhat inhomogeneous along the specimen length at the last stage of extension before fracture. For the present purpose to establish the SOR, Fig. 2c provides adequate information although the extension was terminated by the fracture initialized by an internal inclusion (impurity). Based the results presented in Sections 3 and 4, we think that the fracture in uncut EPDM specimens occurs plausibly either because of impurities (larger than 50 μ m) in the specimen interior or because the ribbon-like specimen preparation introduced edge roughness on the order of 50 μm or higher. Consequently, Cauchy stress $\sigma_{yy} = \Delta \sigma$ at fracture is below 2 MPa, as is the case shown in Fig. 2c. Under rare circumstances, a more impurity-free specimen with more careful sample preparation could reach $\Delta \sigma = 3$ MPa.

Figs. 2d-e show the examples of the retardance buildup at cut tips for PMMA and PET respectively. To determine the local stress

in notched specimens, the RGB variations with distance r to the cut tip in PMMA and PET are compared to the images in Figs. 2a and 2b respectively. Since color is influenced by the choice of light and camera, images in Fig. 2a-b and 2d-e are from the same pair of light and camera. Here locations of maxima, minima, and intersections of RGB values provide straightforward identification of stress. Using PMMA as an example, at location A in Fig. 2d the G-B intersection in the second order is readily discerned from the same feature in the SOR, marked A in Fig. 2a. At low loads where RGB variation are less distinctive, we estimate the local stress based on the approximate ranking and trends of the RGB curves. For example, at location B in Fig. 2d the R value in RGB is somewhat saturated over the rest of the distance from the notch tip. The red curve lies atop the green curve, as green steadily increases towards red. The stress value at point B in Fig. 2a may be an adequate estimate of point B in Fig. 2d. The error introduced to the assignment of local stress by this pseudo-quantitative assignment is on the order of 0.4 to 2 MPa, corresponding to an uncertainty in the measurement of retardance on the order of 10 to 50 nm. Similarly, for PET near an elastic-yielding transition (EYT), the intersections, maxima, and positions marked A-G in Fig. 2e were matched to similar features marked A-G in Fig. 2b.

Accurate determination of local stress as a function of distance r from the notch tip requires the correct identification of the notch edge. With 4K CCD camera attached to a microscope objective lens a resolution in the range of r_b =1–4 μ m per pixel may be achieved. However, because of imperfections due to the cutting procedure, the polymers' mechanical response to the cutting, and slight misalignment of the camera relative to the cut opening, the notch edge usually appears blurry to various degrees. This limits the available spatial resolution to, at best, $r_b \sim 20$ -40 μ m for the thick PMMA specimens, and 20 μ m for PET and EPDM sheets.

2.3. Theoretical analysis

Tensile extension of precut stripes (along y-axis) produces several non-zero stress components. It is straightforward to diagonalize the stress tensor, i.e., to identify the principal stresses σ_1 and σ_2 [14]. Spatial-resolved birefringence measurements to determine $\Delta n(r)$ are ideally suitable to quantify $\Delta \sigma = \sigma_1 - \sigma_2 = \Delta n/C$ around cut tip. In presence of a non-zero shear stress σ_{xy} the principal stress direction rotates away from the drawing direction to an angle α given by $\tan 2\alpha = 2\sigma_{xy}/(\sigma_{yy} - \sigma_{xx})$. The principal stress difference is given by

$$\Delta \sigma = [(\sigma_{yy} - \sigma_{xx})^2 + 4(\sigma_{xy})^2]^{1/2}.$$
 (5)

The Westergaard's solution [15,16] establishes one foundational pillar for linear elastic fracture mechanics (LEFM) [17,18] by prescribing the following explicit form for the quantities in Eq. (5) in presence of an embedded crack of length 2a as

$$\sigma_{yy}(r) - \sigma_{xx}(r) = K_1 f(\theta) / (2\pi r)^{1/2} + \sigma_0,$$
 (6)

$$\sigma_{xy} = K_I h(\theta) / (2\pi r)^{1/2},$$
 (7)

 $\sigma_{zz} = 0$ (plane stress), $\nu(\sigma_{xx} + \sigma_{yy})$ (plane strain) with

$$K_{\rm I} = \sigma_0(\pi a)^{1/2},\tag{8}$$

$$f(\theta) = \sin \theta \sin(3\theta/2),\tag{9}$$

$$h(\theta) = \cos(\theta/2)\sin(\theta/2)\cos(3\theta/2),\tag{10}$$

where θ is the angle formed between the crack propagation direction and the line between cut tip and the observation point. Eq. (6) along with Eq. (9) is the near-tip limit of the full solution [15,18]. A numerical comparison between the full solution and Eq. (6) shows that Eq. (6) accurately reproduces the full solution

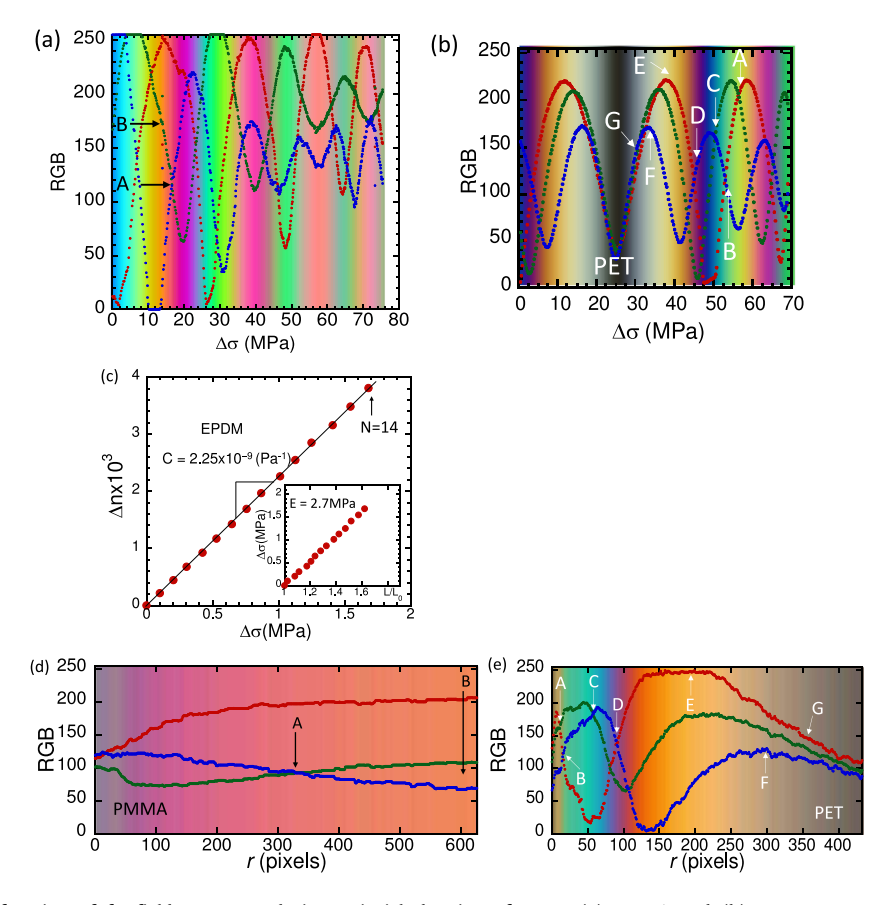


Fig. 2. RGB variation as a function of far-field stress σ_0 during uniaxial drawing of uncut (a) PMMA and (b) PET. Uncut PMMA specimen of dimensions $L_0 \times W_0 \times H_0 = 50 \times 21 \times 5.5 \text{ mm}^3$ was drawn at $V_0/L_0 = 0.2 \text{ min}^{-1}$. Uncut dogbone-shaped PET specimen of dimensions $L_0 \times W_0 \times D_0 = 45 \times 18 \times 0.25 \text{ mm}^3$ was drawn at $V_0/L_0 = 0.1 \text{ min}^{-1}$. (c) Stress-optical relation of EPDM evaluated using Eq. (3) from fringe order N, based on monochromatic light source ($\lambda = 589 \text{ nm}$). The EPDM specimen has an initial thickness of $t_0 = 2.4 \text{ mm}$. Inset figure shows the stress-strain curve, revealing a Young's modulus of $t_0 = 2.7 \text{ MPa}$. (d) RGB variation in pre-cut PMMA as a function of distance $t_0 = 15 \text{ MPa}$. The corresponding image is presented in Fig. 3a. (e) RGB variation in pre-cut PET as a function of $t_0 = 15 \text{ MPa}$. The corresponding image is presented in Fig. 4a. (For interpretation of the references to color in this figure legend, the reader is referred to the web version of this article.)

for r < a/4. The stress fields for single edge notch of size a, which is the experimental configuration of the present study, obey the same expressions in the limit where specimen width W >> a, except for a small correction [17] to Eq. (8), with $K_{\rm I} = 1.12\sigma_0(\pi\,a)^{1/2}$.

The tensile stress field $T(r, \theta) = \sigma_{yy} - \sigma_{xx}$ at crack tip can be solved in terms of the principal stress difference $\Delta \sigma$ given in Eq. (5)

$$T = \sigma_{yy} - \sigma_{xx} = \{ [(1+A^2)(\Delta\sigma)^2 - A^2\sigma_0^2]^{1/2} + A^2\sigma_0 \} / (1+A^2)$$
 (11)

where $A(\theta)$ is given by

$$A(\theta) = 2h/f = \cot(3\theta/2). \tag{12}$$

Since T is an explicit function of $\Delta\sigma$, we can determine T based on the one-to-one correspondence that exists between $\Delta\sigma$ and Δ n via Eq. (4). At $\theta=\pi/3$, $A(\theta)=0$ so that Eq. (11) simply reads

$$T(r, \theta = \pi/3) = \Delta \sigma = \Delta n/C, \tag{13}$$

where the second equality follows from Eq. (4). When monochromatic light is employed, T equals $N(r)f_{\sigma}/t$, where the fringe-stress coefficient $f_{\sigma} = \lambda/C = 0.27$ MPa mm in the case of EPDM. For r < a/4, we can apply Eqs. (6) through (10) to provide an explicit expression for the functional dependence of T on r as

$$\sin(\pi/3)K_1/(2\pi r)^{1/2} + \sigma_0 = T(r, \theta = \pi/3). \tag{14}$$

Such a prediction is to be compared with T in Eq. (13), which can be determined from the birefringence measurements.

3. Results

At room temperature PMMA can undergo brittle fracture without crazing [4,19] when the drawing rate is relatively high. Relative to cut-free specimens, PMMA containing a large precut becomes weaker in presence of a through-cut that causes strain localization. The stress buildup at the cut tip can be quantified using the birefringence observation, based on the setup shown in Fig. 1. Fig. 3a contains a collection of snapshots at different moments from the video recording (video-PMMA in Supporting Information) of a precut PMMA being drawn until fracture. We can present the RGB values as a function distance from the cut tip, as shown in Fig. 3b, in order to describe the stress field according to the combination of Figs. 2a and 2d that correlates RGB and stress. By analyzing images like those in Fig. 3b the actual stress field T around the tip at $\theta = \pi/3$ can be evaluated according to Eq. (13) and plotted as a function of $r^{-1/2}$, as shown in Fig. 3c. The linearity between T(r) and $r^{-1/2}$ shows the experimental data to be in a qualitative agreement with the approximate expression for T in Eq. (14), apart from the fact that the slopes in Fig. 3c reveal an experimental K_{exp} smaller than K_{I} of Eq. (8). The origin of the discrepancy arises from the experimental fact that the stress buildup ceases near the cut tip for all values K_I . The emergence of a stress saturation zone (SSZ) of size r_{ss} , ranging from 0.08 to 0.2 mm, limits the range of the $r^{-1/2}$ scaling of T under the condition of r < a/4. As a consequence, the experimental data in Fig. 3a is mostly in the transitional regime where K_{exp} is

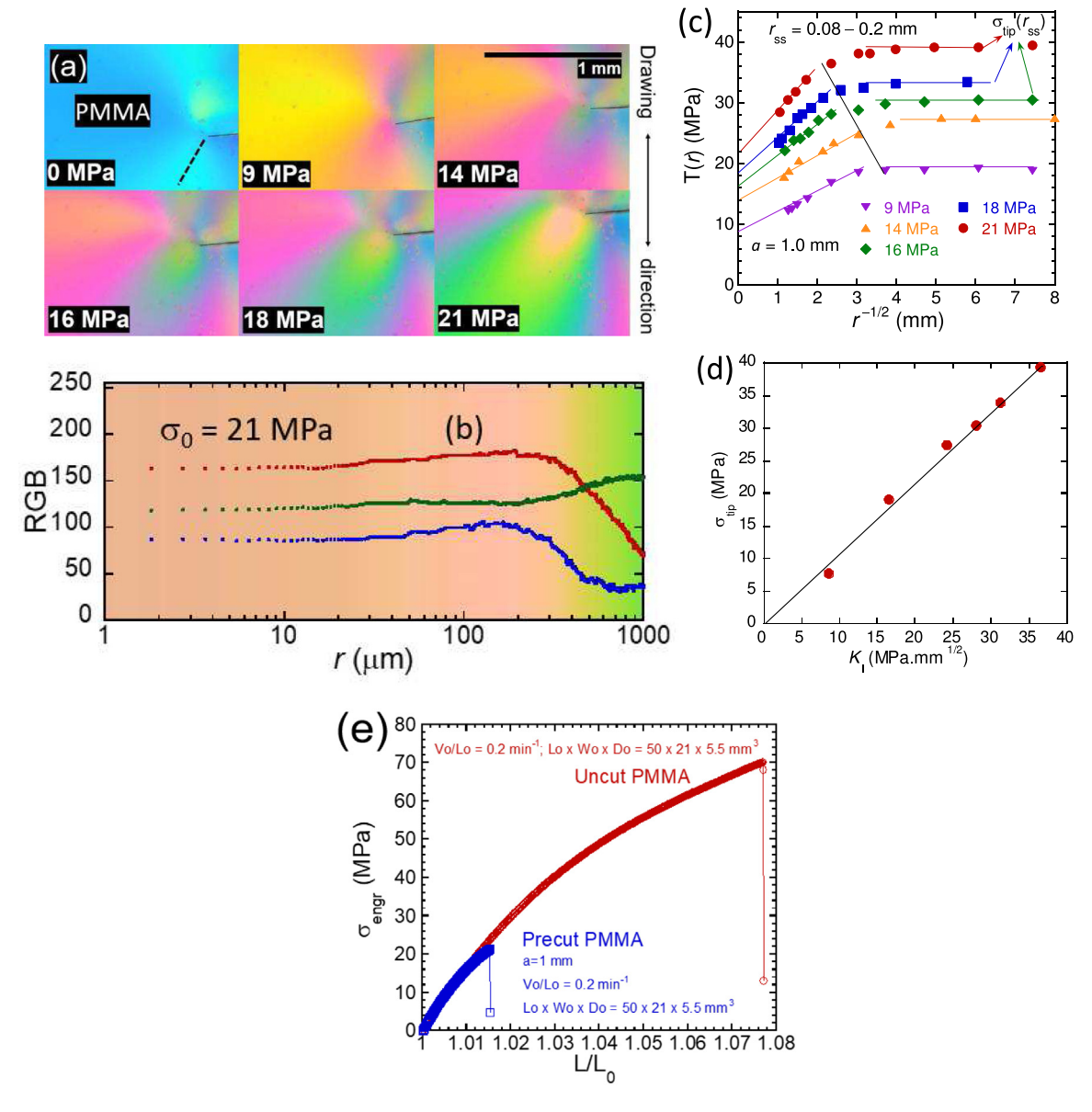


Fig. 3. (a) Images of PMMA specimen ($L_0 \times W_0 \times D_0 = 50 \times 20.8 \times 5.5 \text{ mm}^3$) with single-edge notch (cut length a=1 mm) in birefringence setup of Fig. 1 at different stages during at $V_0/L_0 = 0.2 \text{ min}^{-1}$ to failure. (b) The RGB profile as a function of distance r from tip at $\theta = \pi/3$ for $\sigma_0 = 21 \text{ MPa}$. (c) Local tensile stress T as a function of r at different stages of drawing, corresponding to different values of σ_0 from 0 to 21 MPa, obtained by comparing the RGB profile along the diagonal dashed line (at 60 degrees) at each load σ_0 (0 to 21 MPa) to Fig. 2a. (d) Linear dependence of tip stress as a function of K_1 until fracture. (e) Stress-strain relationship for uncut and precut (a=1 mm) PMMA specimens (E=1.8 GPa). (For interpretation of the references to colour in this figure legend, the reader is referred to the web version of this article.)

necessarily lower than K_1 . Specimens with much larger cut size would reduce the discrepancy.

Besides the discovery of SSZ, there are three more features to note: First, the intercepts reveal a stress level in the far-field that matches the nominal load σ_0 . Second, the local stress level grows with σ_0 in the range from 5 to 21 MPa. Third, the tip stress, i.e., $\sigma_{\rm tip} = T(r=r_{\rm ss})$ increases linearly with $K_{\rm I}$ of Eq. (8) until the point of fracture, as shown in Fig. 3d. For completeness, Fig. 3e provides the stress vs. strain curves from tensile drawing of the uncut and precut specimens.

The linear relation between $\sigma_{\rm tip}$ and $K_{\rm l}$ in Fig. 3d reveals a characteristic length scale P = 0.9 mm. Phenomenologically, we can simply define their relation as

$$\sigma_{\text{tip}}(K_{\text{I}}) = T(r_{\text{ss}}) = \Delta n(r = r_{\text{ss}})/C = K_{\text{I}}/P^{1/2}.$$
 (15)

Detailed analysis shows [20] that in the limit of P << a P would be $2\pi r_{ss}$ independent of the cut length a. Data in Fig. 3d show P

to be not far from $2\pi r_{ss}$, given the range of the r_{ss} indicated in Fig. 3c.

It is necessary to point out that the theoretical expression Eq. (14) does not anticipate such stress saturation (SS). Since the SS as well as the linearity between $\sigma_{\rm tip}$ and $K_{\rm I}$ both take place well before the onset of fracture, the SSZ seems to involve a different concept from Irwin's plastic zone concept. In order to find out whether or not these two features are universal for glassy polymers, we investigate a ductile polymer, i.e., amorphous PET, because we expect LEFM to apply before the onset of yielding at the cut tip.

In presence of sizable precut with a=4.6, PET specimen of length L_0 =100 mm is drawn at a speed of V_0 =10 mm/min. Video recording captures the birefringence buildup due to the cut, as shown in video-PET in Supporting Information that produces the images in Fig. 4a. Referring to Figs. 2b and 2e, the local stress field can be determined relative to the distance r from the cut

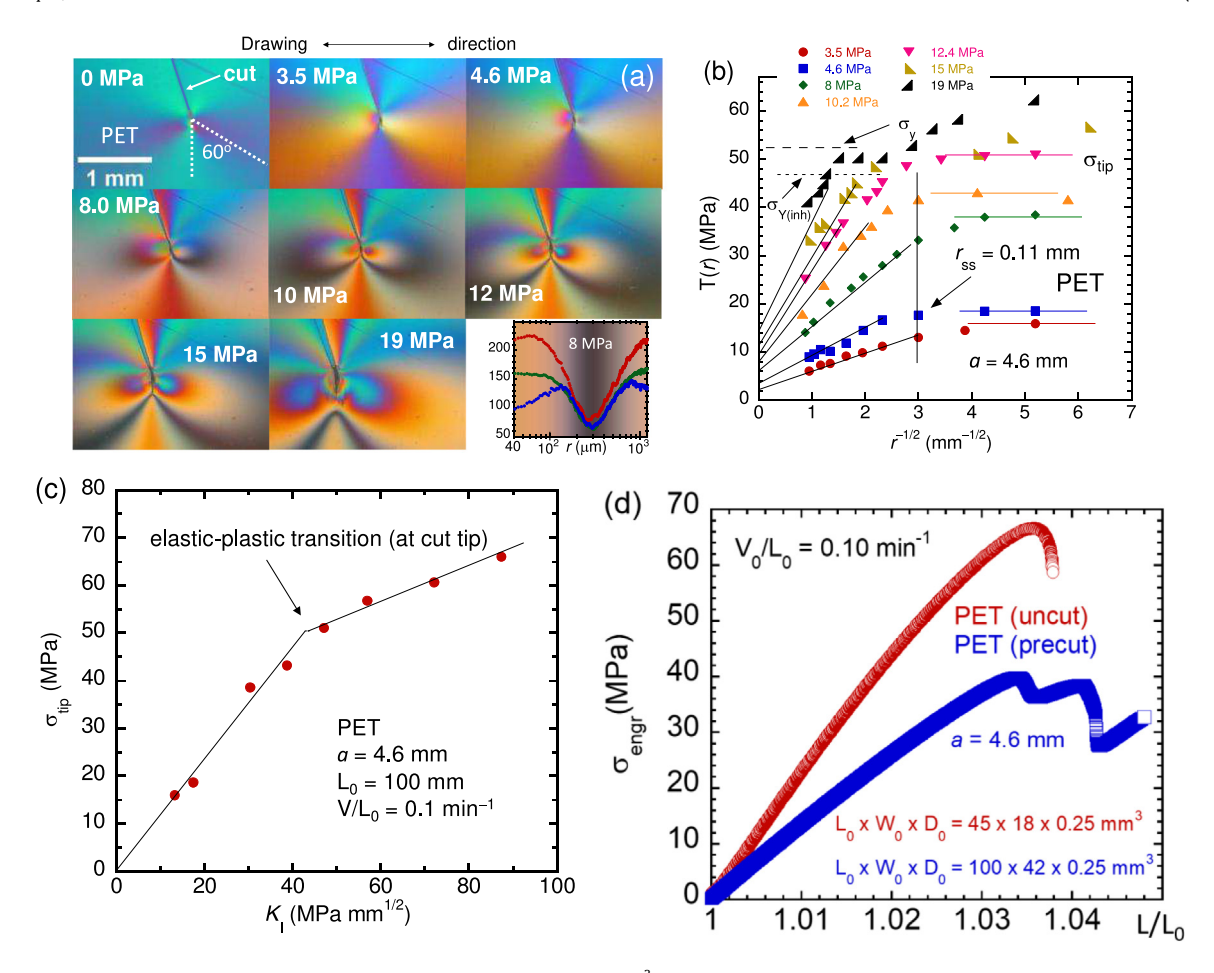


Fig. 4. (a) Images of precut PET specimen ($L_0 \times W_0 \times D_0 = 100 \times 42 \times 0.25 \text{ mm}^3$) with size a = 4.6 mm at different stages during drawing at $V_0/L_0 = 0.10 \text{ min}^{-1}$. The last image indicates how the RGB profile varies as a function of r, the distance from the tip. (b) The RGB profile along the diagonal dashed line (60 degrees) at each load was compared to Fig. 2b to obtain local tensile stress T(r), plotted against $r^{-1/2}$. (c) Tip stress read from the stress plateau in (b) is plotted against K_1 of Eq. (8). (d) Stress–strain curves of PET (E = 2.3 GPa in the uncut specimen). The precut ribbon–shaped specimen (blue) was not drawn to failure. (For interpretation of the references to colour in this figure legend, the reader is referred to the web version of this article.)

tip, as shown in Fig. 4b, at different values of σ_0 . Beyond σ_0 10 MPa, the cut tip shows sign of yielding, revealing a level of inherent yield stress $\sigma_{Y(inh)}$ as shown. On the other hand, up to $\sigma_0 = 12.4$ MPa, the observed tip stress does not exceed the yield stress $\sigma_{\rm y}$ (ca. 52 MPa) measured from a cut-free PET, yet T(r) levels off for $r^{-1/2}$ > 3 mm^{-1/2} to reveal a SSZ. The tip stress $\sigma_{\rm tip}$ in the SSZ monotonically increases with σ_0 . However, unlike PMMA that undergoes brittle fracture to terminate the linearity between σ_{tip} and K_I (cf. Fig. 3d), Fig. 4c shows a kink to indicate an elastic-plastic transition (EPT) at the cut tip. This EPT is confirmed by observation of residual birefringence upon unloading at $\sigma_0 =$ 15 MPa that corresponds to the second point after the kink in Fig. 4c. Moreover, the emergence of stress plateau before the EPT further indicates that the SSZ for PET with $\sigma_0 \leq 12.4$ MPa as well as for PMMA before fracture is not associated with the Irwin's concept of plastic zone. In other words, since no yielding occurs at the tip below 12 MPa, the observation is in contradiction with Dugdale model [21] that predicts emergence of tip yielding to start at a vanishingly low load σ_0 .

Similar to Fig. 3d, the first slope in Fig. 4c corresponds to P=0.71 mm according to Eq. (15), in quantitative agreement with $2\pi r_{\rm ss}$ identified in Fig. 4b. For completeness, the stress vs. strain curves of both uncut and precut specimens are presented in Fig. 4d.

The birefringence method for determination of local stress field near crack tip is also useful in a study of fracture of elastomers. In the present study, we examine a crosslinked rubber based on EPDM. Given the high level of retardance in the thick EPDM sheets, monochromatic sodium (low pressure) lamp was employed to avoid color saturation. Specifically, we quantify the stress field T(r) by reading the fringe orders (N or $N + \frac{1}{2}$) at the cut tip from video recording (Video-EPDM in Supporting Information). The values of N(r) for different r at various levels of σ_0 , as those shown in the photos in Fig. 5a, are inserted in Eq. (13) via Eqs. (3)-(4) to obtain T. The spatial variation of birefringence is explicitly displayed in Fig. 5b, analogous to Fig. 3b, showing that there is no higher order beyond N = 11 within a distance of 20 µm from the tip. At different stages of drawing, we obtain a family of corresponding curves showing how T varies with $r^{-1/2}$ as shown in Fig. 5c. The most significant feature revealed in Fig. 5c is that the $r^{-1/2}$ scaling of T terminates upon approaching the tip, i.e., there also exists a kink in the plot of T vs. $r^{-1/2}$. This character of stress saturation is similar to that shown in Fig. 3c and Fig. 4b, with r_{ss} around 0.05 mm, i.e., about half of that seen in PMMA and PET. Since unloading test reveals no discernible residual birefringence, as can be expected from an elastomer (rather than a glassy polymer), the emergence of the SS zone in EPDM is not a plastic zone suggested in Irwin's theory to cope with the stress singularity.

If Eq. (14) accurately depicts the data in Fig. 5c, the intercepts should be σ_0 . We find that the intercept is indeed numerically close to σ_0 . We can also evaluate $K_{\rm exp}$ from the initial slope based on the data in Fig. 5c. Fig. 5d shows a close agreement between $K_{\rm exp}$ and the operational $K_{\rm I}$ of Eq. (8), suggesting that Eq. (14)

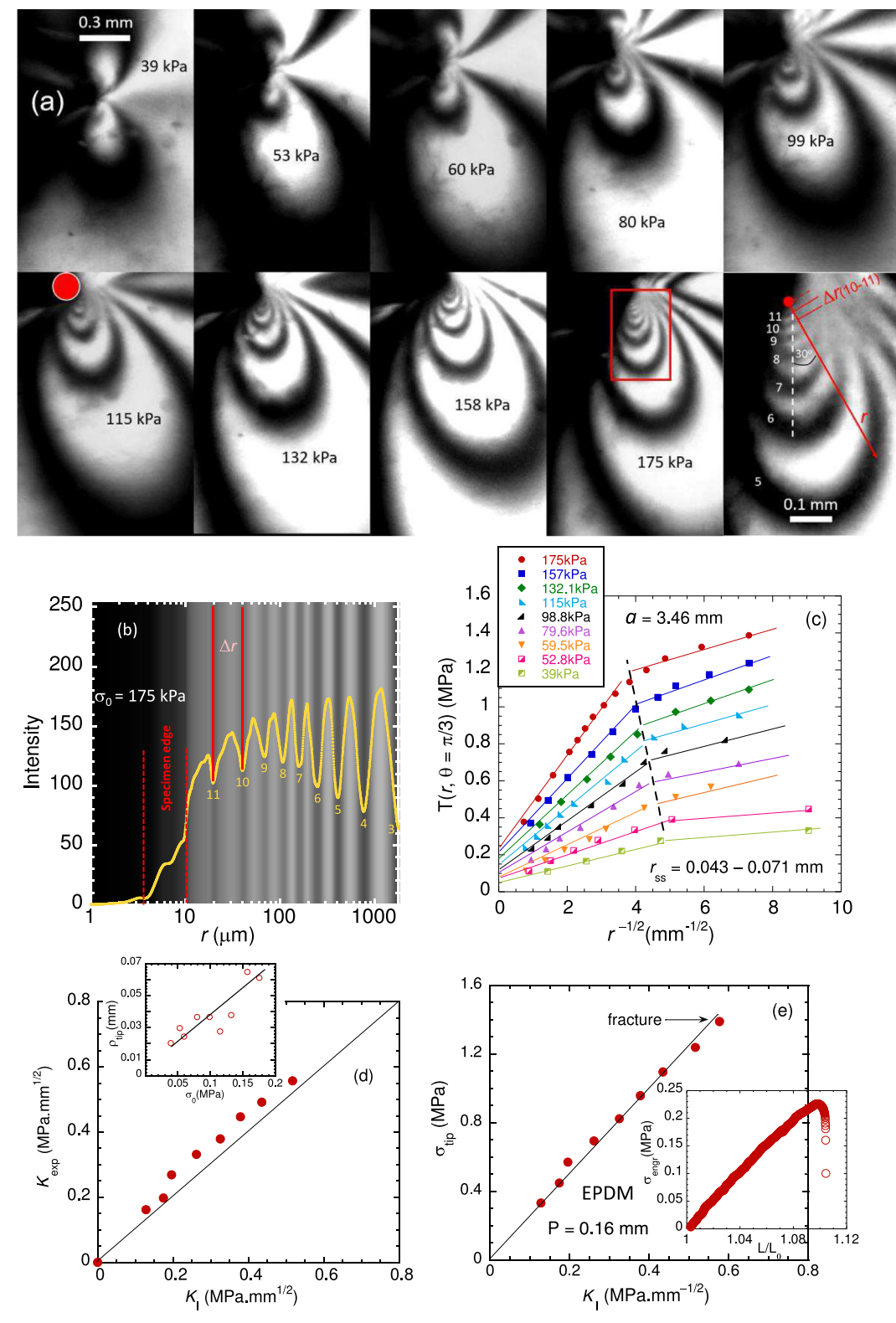


Fig. 5. (a) Images of precut EPDM ($L_0 \times W_0 \times D_0 = 50 \times 15 \times 2.54 \text{ mm}^3$) with size a = 3.46 mm in birefringence setup of Fig. 1 (monochromatic sodium lamp without retardation plate) at different stages during drawing at strain rate $V/L = 0.05 \text{ min}^{-1}$. The sixth image at 115 kPa contains a (red color online) circle at the cut tip used to estimate the radius of local curvature, which is a method applied for all other images. The tenth image, being an enlarged region of ninth image, shows the fringe order N up to 11 and describes how r = 0 was conservatively chosen so that the claimed resolution is a lower bound: Given the last resolvable neighboring fringe orders of 10 and 11, their separation $\Delta r = 20 \mu \text{m}$ is used to locate r = 0, which $20 \mu \text{m}$ away from N = 11, as shown. (b) The gray scale profile as a function of distance r from tip at $\theta = \pi/3$ corresponding to the tenth image in (a). The edge of the specimen is approximately at r = 4-10 μm, as indicated by the two dashed lines. (c) Local tensile stress T as a function of $r^{-1/2}$. T is calculated in two steps: Reading fringe orders N and half-orders N + 1/2 at different values of r from images in (a) to insert into Eq. (3) for Δn and evaluating T using Eqs. (4) and (13). The data reveal emergence of stress saturation zone of size $r_{\rm ss}$ at the kinks. (d) $K_{\rm exp}$ evaluated from the first slopes in (c) at different values of $K_{\rm I}$ of Eq. (8), plotted against $K_{\rm I}$. At the onset of crack propagation, the critical $K_{\rm Ic}$ is 0.58 MPa mm^{1/2}. Inset figure shows the variation of the radius of curvature, $\rho_{\rm tip}$, as a function of the nominal load $\sigma_{\rm O}$. (e) Tip stress read from the stress plateau in (c) as a function of $K_{\rm I}$ where the inset shows the stress vs. strain curve of the precut specimen that fractures at $L/L_0 = 1.07$ and $\sigma_{\rm c} = 0.174 \text{ MPa}$, which is identical to that of an uncut specimen, given in the inset of Fig. 2c. (For interpretation of the references to co

is a good approximation to the full Westergaard solution [20]. EPDM also confirms another important characteristic in Fig. 5e that has been seen in Figs. 3d and 4c, i.e., the tip stress as well as birefringence increases linearly with the stress intensity factor $K_{\rm I}$. According to Eq. (15), the linearity in Fig. 5e defines a length scale P = 0.16 mm, not far from $2\pi r_{\rm ss}$ identified in Fig. 5c. An examination of kink location in Fig. 5c and inset in Fig. 5d shows that the variation of $r_{\rm ss}$ originates from that of the radius of curvature $\rho_{\rm tip}$ at the cut tip, which monotonically increases with load. We had a similar observation of P $\sim 2\pi r_{\rm ss}$ for PMMA and PET.

4. Discussion

Since EPDM undergoes large strain, the data in Fig. 5c require clarification. Theoretical studies [22,23] in the literature indicate more complicated stress fields near the crack tip in presence of large deformation than those prescribed by Eqs. (6) through (10). The position given by $(r, \theta = \pi/3)$ refers to the tip, i.e., r = 0 at the tip. Thus, at the different loads from 39 to 175 kPa, we did not report the birefringence of the various material points. If Fig. 5c is to be compared with theoretical description based on the deformed configuration, there would be small errors. Using particle-tracking, we confirmed that within a distance of 1 mm from the cut tip, the material points along $\theta = \pi/3$ did not move by more than 10%. Thus, the data in Fig. 5c could be stated to be accurate with 10% error, leaving our conclusion completely unaffected.

Because of the stress saturation on length scales well resolvable by our optical observation, the spatial variation of birefringence near crack tip at different stages including the point of fracture has been conveniently characterized. Since our PMMA and EPDM specimens are rather thick, over 5 and 2 mm respectively, the condition at precut tip is certainly plane strain. Since the polarized light was sent along Z axis the emergence of triaxial stress state does not obscure the birefringence measurements. However, since the stress-optical relation (SOR) acquired from uniaxial extension of uncut specimen involves plane stress, the use of SOR to convert tip birefringence to tensile stress is imprecise. At fracture, we have taken $\sigma_{\rm tip}(K_{\rm Ic})$ as the inherent strength $\sigma_{\rm Eliph}$.

Taking the last data points in Fig. 3d and Fig. 5e as $\sigma_{\text{F(inh)}}$ we note that in either case $\sigma_{\text{F(inh)}}$ might be lower than σ_{b} , which is the fracture strength or breaking stress of uncut specimen, given by the last point of Fig. 3e showing 70 MPa for PMMA and the last point of the inset in Fig. 2c showing 1.7 MPa for EPDM. The assumption of $\sigma_{\text{F(inh)}} < \sigma_{\text{b}}$ (under plane stress) is reasonable because $\sigma_{\text{F(inh)}}$ is upper-bounded by the inherent strength σ^* under plane stress and σ_{b} is also upper bounded by σ^* . Fracture in PMMA and EPDM requires higher stress in plane stress because the chain network (associated with either intermolecular uncrossability or crosslinking) is free to contract along the specimen thickness direction (Z axis) – the lack of contraction under plane strain may either lower the threshold for chain pullout in PMMA or cause more chain stretching towards scission in EPDM.

The linear increase of the tip stress with $K_{\rm I}$, as shown in Fig. 3d and Fig. 5e, holds true all the way to the onset of crack propagation, i.e., Eq. (15) is valid at fracture. Equating $\sigma_{\rm tip}(K_{\rm Ic})$, i.e., the tip stress at fracture, with $\sigma_{\rm F(inh)}$, the following expression shows that the critical stress intensity factor $K_{\rm Ic}$

$$K_{\rm lc} = \sigma_{\rm F(inh)} P^{1/2} \tag{16}$$

is determined by two material parameters. Here $\sigma_{F(inh)}$ should be regarded as a material constant. Thus, K_{Ic} would be as a material constant if P in Eq. (16) is material-characteristic. It can be shown by making a large number of precut PMMA specimens that K_{Ic}

varies [5] from 0.8 to 1.4 MPa m^{1/2}, corresponding to P in Eq. (16) varying from 0.6 to 1.2 mm, given $\sigma_{F(inh)} = 40$ MPa from Fig. 3d. In other words, the variation in K_{Ic} for PMMA can be traced to that in P. Fig. 5c and inset in Fig. 5d shows the variation to arise from the cut characteristic, i.e., radius of curvature ρ_{tip} . It is reasonable to assert that P in Eq. (16) is given by the geometric characteristics of the tip, e.g., the tip being partially through-thickness in the case of thick PMMA, or the tip turning blunter during drawing in the case of EPDM.

In LEFM, K_{lc} is usually determined from specimens containing through-cuts and is therefore a function of how the precut is made. Some cuts have more blunt tips than others so that the local curvature at the tip is a variable. Theoretical analyses and finite-element calculations [24-27] have shown that the local stress saturates upon approaching the tip due to the finite curvature. The SS zone revealed by our experiments on PMMA and EPDM has little in common with the concept of Irwin plastic zone that is commonly invoked within the second pillar of fracture mechanics to cope with the mathematical stress singularity. For polymers under current investigation, the intentional cut is never sharp enough to call for Irwin's remedy-plastic zone formation. For a given cutting method, the value of ρ_{tip} is inherent to the material. It is in this sense that P is also characteristic of the material under study. In passing, we note that the effect of tip bluntness on impact strength is well documented, and such effect has been suggested to imply that tip stress is a controlling parameter for fracture [4].

Energy balance argument of Griffith [1] and Irwin [28] prevails because little is generally known about the stress state at crack tip. The stress intensification approach [15,29] resorts back to the energy balance argument because the prediction of stress singularity at cut tip forces one [30] to give up any attempt to arrive at a local fracture criterion based on the stress state at the tip. Specifically, the second pillar suggests that fracture is controlled by the stress intensity factor $K_{\rm I}$ in Eq. (8). Since $G_{\rm I}$ and $K_{\rm I}$ are related as $G_{\rm I} = K_{\rm I}^2/E$, stating that fracture occurs at K_{lc} is equivalent to saying Eq. (2) is the condition for fracture. Therefore, G_{lc} is usually the only parameter evaluated at fracture and is taken as the fracture criterion: G_{I} needs to exceed G_{Ic} for fracture to take place. On the other hand, Eq. (2) only indicates how to measure G_{lc} by examining a precut specimen with cut length a and by recording its fracture stress $\sigma_{\rm c}$. But we do not know what determines G_{lc} and why G_{lc} is of the value as revealed by experiment of polymers. This is in sharp contrast to materials such as silica glasses where one could argue G_{lc} is given by surface fracture energy Γ .

When G_{lc} varies by a factor of three for PMMA as shown by Berry [5], we are at loss about the origin of this variation. Eq. (16) shows how G_{lc} is actually dependent on local conditions at crack tip as

$$G_{lc} = (K_{lc})^2 / E = 2P\{[\sigma_{F(inh)}]^2 / 2E\},$$
 (17)

where the quantity inside the curled brackets may be regarded as the work density of fracture $w_{\rm F}$ for an uncut specimen if $\sigma_{\rm F(inh)}{\sim}\sigma_{\rm b}$. Eq. (17) points at the origin of toughness $G_{\rm Ic}$, as Eq. (16) does for $K_{\rm Ic}$. Since the radius of curvature of cut tip $\rho_{\rm tip}$ prescribes the magnitude of P, we can conclude that toughness defined either in terms of $G_{\rm Ic}$ or $K_{\rm Ic}$ is characterized by inherent strength $\sigma_{\rm F(inh)}$ and cut characteristic $\rho_{\rm tip}$. Specifically, the spread of $G_{\rm Ic}$ by a factor of three for PMMA⁵ is plausibly due to a variation in P.

Finally, it is instructive to combine the operational definition Eq. (8) for $K_{\rm I}$ with Eq. (16) and indicate the relation between global and local stress states, i.e., to "predict" the fracture stress in a precut specimen as

$$\sigma_{\rm c} = \sigma_{\rm F(inh)} (P/\pi a)^{1/2},\tag{18}$$

revealing the proportionlity constant in $\sigma_c \propto a^{-1/2}$ is determined by $\sigma_{F(\text{inh})}$ and P. This expression also reveals the meaning of σ_c . At σ_c the stress at the crack tip has intensified by a factor of $(\pi a/P)^{1/2}$ to reach the level of inherent strength.

5. Summary and conclusion

Using spatial-resolved birefringence measurements of polymers in either amorphous glassy or elastomeric state, we have demonstrated the elusive connection between global and local mechanical characteristics during fracture. For example, toughness given in terms of global features (i.e., far-field stress and cut length) is shown to relate to the material physics at the crack tip of given sharpness, i.e., the tip stress reaching inherent strength. Thus, for brittle plastics such as PMMA and elastomers in the example of EPDM, we have provided a much needed and longwaited explanation for why toughness appears to be a material constant, or more broadly, why linear elastic fracture mechanics can successfully capture the essence of fracture, e.g., the critical load σ_{c} for fracture in a precut specimen scaling with the cut length a as $a^{-1/2}$. In other words, for polymers we have identified pertinent parameters that quantify the magnitude of toughness so that the prefactor in $\sigma_{\rm c}\sim a^{-1/2}$ can be prescribed. Specifically, toughness (cf. Eq. (16) or (17)) is given by a combination of inherent strength and radius of curvature of intentional cut. Related to this conclusion is the finding, for brittle polymers, that the breaking strength (stress) σ_b of cut-free polymers is on the same order of magnitude as the inherent strength $\sigma_{\text{F(inh)}}$, provided inherent strength does not vary greatly between plane stress (σ^*) and plane strain (σ^{\dagger}).

We resort to fracture mechanics whenever we inquire about mechanical behavior in presence of large cracks. When crack tip is blunt, as is often the case for intentional through-cuts that experimenters routinely make, the tip stress is rather low at early stage when nominal load σ_0 is low, unlike the assumption of LEFM, and grows approximately linearly with σ_0 . Moreover, the local stress tends to plateau as the tip is approached within a distance r_{ss} that is comparable to the radius of curvature ρ_{tip} of the tip. Such features allow us to determine the maximum stress at crack tip upon fracture through birefringence observations and demonstrate an explicit relationship in Eq. (16) for toughness. For both glassy polymers (PMMA and PET) and elastomeric EPDM, $r_{\rm ss}$ is in the range of 0.04 to 0.2 mm, which prescribes K_{lc} because P in Eqs. (16)–(17) seem to be controlled by r_{ss} , which is dependent on the geometric characteristics of the crack tip. In other words, Eq. (17) shows why toughness G_{lc} is of a certain magnitude, set by the value of P. Although P varies to a degree, it is material specific. Because of the observed stress saturation at the tip, we conclude that PMMA and EPDM may be flaw tolerant as long as defects or impurities are appreciably below $r_{\rm ss}$ \sim 50 μ m. At this juncture, it is necessary to indicate the cuts of other sizes in PMMA and EPDM have been introduced and the corresponding precut specimens have been found to produce data that collapse onto Fig. 3c and Fig. 5e respectively, suggesting that brittle fracture commences when the tip stress reaches a common value independent of cut length a. It remains unknown whether this conclusion applies to all brittle polymers. Only further investigation can begin to address such a question.

At the present, while we have relatively good theoretical understanding of how $\sigma_{F(ihn)}$ may be related to the structure of the chain networking and how to increase $\sigma_{F(inh)}$ for glassy polymers [7], it is less clear how to increase $\sigma_{F(inh)}$ for crosslinked rubbers. Separately, toughness can also increase according to Eq. (16) and Eq. (17) if P increases. The introduction of a sacrificial network [31,32] to construct double-network in hydrogels [33–35] may have partially achieved the goal by increasing P. It remains to

be demonstrated whether strain-induced crystallization actually causes tip blunting to increase the toughness of vulcanized natural rubbers by increasing P in Eq. (16)–(17). Future studies may also explore fatigue failure of polymers in light of the present results. Since available phenomenology suggests $G_{\rm I}$ to be a pertinent parameter controlling fatigue, it is desirable to find out in the case of elastomers whether a threshold $G_{\rm IO} < G_{\rm IC}$ can also be expressed in a way similar to Eq. (17) for $G_{\rm IC}$. As an activated processes, we expect fatigue to be understood in terms of the relationship between the barrier lowering and induction time. For example, more cycles are required for crack growth under a lower load.

Finally, we remark that for EPDM elastomer $G_{\rm lc}$ is conventionally evaluated from the Rivlin-Thomas formula [36–38]: $G_{\rm lc(RT)}=6w(\lambda_c)a/\sqrt{\lambda_c}$, where λ_c is the critical draw ratio at fracture, and w is the strain energy density, obtainable from the area under the stress vs. strain curve, e.g., inset of Fig. 2c. We found $G_{\rm lc(RT)}=6\times(0.07\times0.174/2)\times10^3\times3.46\times1.07^{-1/2}=122~{\rm J/m^2}.$ On the other hand, Eq. (17) gives $G_{\rm lc}=[(0.58)^2/2.7]\times10^3=125~{\rm J/m^2}.$ Such an excellent agreement may be taken to imply that Eq. (17) holds true for this elastomer. This is unsurprising given the fact that the fracture strain of $\lambda_c=1.07$ is rather small. In other words, the agreement takes place because the present EPDM is not highly stretchable, and tip blunting is insignificant.

CRediT authorship contribution statement

Travis Smith: Development of quantitative birefringence measurements, Data curation on PET, Formal analysis, Validation, Writing – review & editing. **Chaitanya Gupta:** Development of quantitative birefringence measurements, Data curation on PMMA, Formal analysis, Validation, Writing – review & editing. **Zehao Fan:** Development of quantitative birefringence measurements, Data curation on EPDM, Formal analysis, Validation, Writing – review & editing. **Gregory J. Brust:** Synthesis of EPDM. **Russ Vogelsong:** Synthesis of EPDM. **Caleb Carr:** Development of quantitative birefringence measurements. **Shi-Qing Wang:** Supervision, Conceptualization, Methodology, Formal analysis, Validation, Writing – original draft, Writing – review & editing.

Declaration of competing interest

The authors declare that they have no known competing financial interests or personal relationships that could have appeared to influence the work reported in this paper.

Acknowledgments

This work is supported, in part, by the Polymers program at the National Science Foundation, United States of America (DMR-1905870, 2210184) that also provided REU supplemental funding for CC's summer research internship in the NSF REU-2051052 program at University of Akron. SQW acknowledges many email exchanges with Dr. Zhigang Suo, from whom he learned the essentials of fracture mechanics. Finally, we thank Dr. X. Yu in Auriga Polymers Inc. for providing us the PET sheets.

Appendix A. Supplementary data

Supplementary material related to this article can be found online at https://doi.org/10.1016/j.eml.2022.101819. Video-uncut EPDM: Uniaxial extension of ribbon like EPDM specimen involving the setup of Fig. 1 with sodium light.

Video-PMMA: Taken with a C-mount zoom-lens (Edmund Optics) at $2.5\times$ mounted on a digital camera (Mokose C100) based on a setup sketched in Fig. 1 to provide the images at 4K resolution, used in Fig. 3 to quantify the local stress field around cut tip. The field of view of this video is $3.47\times1.95~\text{mm}^2$.

Video-PET: Taken with a micro-lens ($2.5\times$) mounted on CCD camera based on a setup sketched in Fig. 1 to provide the images used in Fig. 4 to quantify the local stress field around cut tip. The field of view is 2.65×1.77 mm².

Video-EPDM: Taken with a C-mount zoom-lens (Hayear model HY-180XA) at $4.5 \times$ mounted on a digital camera (Mokose C100) based on a setup sketched in Fig. 1 to provide the images at 4K resolution, used in Fig. 5 to quantify the local stress field around cut tip. The field of view is 3.13×1.76 mm².

References

- [1] A. Griffith, A. VI, The phenomena of rupture and flow in solids, Philos. Trans. R. Soc. Lond. Ser. A Contain. Pap. A Math. Phys. Charact. 221 (582–593) (1921) 163–198.
- [2] C.B. Bucknall, Toughened Plastics, Springer, 1977.
- [3] I.M. Ward, J. Sweeney, Mechanical Properties of Solid Polymers, third ed., John Wiley & Sons, Ltd, Chichester, UK, 2012.
- [4] A.J. Kinloch, Fracture Behaviour of Polymers, Springer Science & Business Media, 2013.
- [5] J. Berry, Fracture processes in polymeric materials. I. The surface energy of poly (methyl methacrylate), J. Polym. Sci. 50 (153) (1961) 107–115.
- [6] J. Berry, Fracture processes in polymeric materials. II. The tensile strength of polystyrene, J. Polym. Sci. 50 (154) (1961) 313–321.
- [7] S.-Q. Wang, S. Cheng, P. Lin, X. Li, A phenomenological molecular model for yielding and brittle–ductile transition of polymer glasses, J. Chem. Phys. 141 (9) (2014) 094905.
- [8] S.Q. Wang, S.W. Cheng, Experiments-inspired molecular modeling of yield-ing and failure of polymer glasses under large deformation, chapter 12, in: C. Roth (Ed.), Polymer Glasses, CRC Press, 2016, pp. 395–423.
- [9] P.I. Vincent, A correlation between critical tensile strength and polymer cross-sectional area, Polymer 13 (12) (1972) 558–560.
- [10] S.-Q. Wang, On chain statistics and entanglement of flexible linear polymer melts, Macromolecules 40 (24) (2007) 8684–8694.
- [11] G. Lake, A. Thomas, The strength of highly elastic materials, Proc. R. Soc. Lond. Ser. A Math. Phys. Eng. Sci. 300 (1460) (1967) 108–119.
- [12] A. Tagaya, H. Ohkita, T. Harada, K. Ishibashi, Y. Koike, Zero-birefringence optical polymers, Macromolecules 39 (8) (2006) 3019–3023.
- [13] H. Shafiee, A. Tagaya, Y. Koike, Mechanism of generation of photoelastic birefringence in methacrylate polymers for optical devices, J. Polym. Sci. B Polym. Phys. 48 (19) (2010) 2029–2037.
- [14] E. Hearn, Mechanics of Materials, Vols. 1-2, Pergamon Press, Headington Hill Hall, Oxford OX 3 0, BW, UK, 1985, 1985.
- [15] H.M. Westergaard, Bearing pressures and cracks, Trans. AIME J. Appl. Mech. 6 (1939) 49–53.
- [16] G.R. Irwin, Analysis of stresses and strains near the end of a crack traversing a plate, 1957.
- [17] T.L. Anderson, Fracture Mechanics: Fundamentals and Applications, CRC Press, 2017.
- [18] C.-T. Sun, Z. Jin, Fracture Mechanics, Academic Press, 2011.

- [19] R.N. Haward, R.J. Young, The Physics of Glassy Polymers, Springer, Netherlands, 1997.
- [20] S.Q. Wang, T. Smith, C. Gupta, Z. Fan, Fracture mechanics of polymers informed from local stress state, 2022, Review article, unpublished.
- [21] D.S. Dugdale, Yielding of steel sheets containing slits, J. Mech. Phys. Solids 8 (2) (1960) 100–104.
- [22] R. Long, C.-Y. Hui, Crack tip fields in soft elastic solids subjected to large quasi-static deformation A review, Extrem. Mech. Lett. 4 (2015) 131–155
- [23] R. Long, M. Lefranc, E. Bouchaud, C.-Y. Hui, Large deformation effect in mode I crack opening displacement of an agar gel: A comparison of experiment and theory, Extrem. Mech. Lett. 9 (2016) 66–73.
- [24] G. Glinka, Calculation of inelastic notch-tip strain-stress histories under cyclic loading, Eng. Fract. Mech. 22 (5) (1985) 839–854.
- [25] G. Glinka, A. Newport, Universal features of elastic notch-tip stress fields, Int. J. Fatigue 9 (3) (1987) 143–150.
- [26] P. Lazzarin, R. Tovo, A unified approach to the evaluation of linear elastic stress fields in the neighborhood of cracks and notches, Int. J. Fract. 78 (1) (1996) 3–19.
- [27] S. Filippi, P. Lazzarin, R. Tovo, Developments of some explicit formulas useful to describe elastic stress fields ahead of notches in plates, Int. J. Solids Struct. 39 (17) (2002) 4543–4565.
- [28] G.R. Irwin, Onset of fast crack propagation in high strength steel and aluminum alloys, in: Sagamore Research Conference Proceedings, 1956, pp. 289–305.
- [29] G.R. Irwin, Analysis of stresses and strains near the end of a crack transversing a plate, Trans. ASME Ser. E J. Appl. Mech. 24 (1957) 361–364.
- [30] Kinloch stated in his book on page 88: From Eq. (6)-(8) it is evident that as r approaches 0 then the stress approaches infinity and hence stress alone does not make a reasonable local fracture criterion. Therefore, since the level of $K_{\rm I}$ uniquely defines the stress field around the crack, Irwin postulated that the condition $K_{\rm I} > K_{\rm Ic}$ represented a fracture criterion.
- [31] J. Slootman, V. Waltz, C.J. Yeh, C. Baumann, R. Gostl, J. Comtet, C. Creton, Quantifying rate- and temperature-dependent molecular damage in elastomer fracture, Phys. Rev. X 10 (4) (2020).
- [32] Y.J. Chen, G. Sanoja, C. Creton, Mechanochemistry unveils stress transfer during sacrificial bond fracture of tough multiple network elastomers, Chem. Sci. 12 (33) (2021) 11098–11108.
- [33] J.P. Gong, Y. Katsuyama, T. Kurokawa, Y. Osada, Double-network hydrogels with extremely high mechanical strength, Adv. Mater. 15 (14) (2003) 1155–1158.
- [34] J.P. Gong, Why are double network hydrogels so tough? Soft Matter 6 (12) (2010) 2583–2590.
- [35] J.-Y. Sun, X. Zhao, W.R. Illeperuma, O. Chaudhuri, K.H. Oh, D.J. Mooney, J.J. Vlassak, Z. Suo, Highly stretchable and tough hydrogels, Nature 489 (7414) (2012) 133–136.
- [36] R. Rivlin, A.G. Thomas, Rupture of rubber. I. Characteristic energy for tearing, J. Polym. Sci. 10 (1953) 291–318.
- [37] H. Greensmith, Rupture of rubber. X. The change in stored energy on making a small cut in a test piece held in simple extension, J. Appl. Polym. Sci. 7 (1963) 993–1002.
- [38] C. Creton, M. Ciccotti, Fracture and adhesion of soft materials: a review, Rep. Prog. Phys. 79 (2016) 046601.